

Chapter 4

Computational Simulations of Experimental Techniques

4.1 Introduction

The number of experimental techniques and their capability to measure and image magnetic behaviour is constantly increasing along with the ability to computationally simulate different magnetic structures [74, 75]. However, there is still a lack of easily available, well known software for comparing computational predictions of magnetic structures with experimental measurements. This chapter aims to help start filling this gap by utilising modelling to predict the result of some experiments and hence give experimentalists a prediction to compare results against. While there are some software packages available to do this for experiments such as LTEM [76], these usually pertain to only simulating a single technique. Most software for simulations of experiments belong to specific research groups and are not readily available. This chapter details how a simulation software package has been developed in Python to be readily available for simulations of techniques such as LTEM, MFM, x-ray holography and SANS. Focus has been placed on the versatility and ease of integration with micromagnetic programs such as Ubermag [77]. The most up-to-date version of the code is available at Ref. [78].

There are many different techniques for imaging and determining magnetic structures in materials. Table 4.1 summarises a handful of techniques highlighting the important features. While there are a plethora of techniques capable of measuring magnetism and magnetic properties, focus has been placed on the techniques listed in Table 4.1 as they are in common use, with scope for further additions at a later stage.

Table 4.1: Imaging techniques for magnetic structures based on Ref. [75].

	MFM	LTEM	Electron Holography	X-ray Holography
Contrast Origin	$\nabla \mathbf{B}$	\mathbf{B}	Phase shift	\mathbf{M}
Approximate resolution	40 nm	5 nm	5 nm	15 nm
Acquisition time	5-30 min.	0.01-10 sec.	0.01-10 sec.	0.01 sec
Sample thickness	N/A	< 150 nm	< 150 nm	< 200 nm

4.2 Magnetic Structure Setup

For all of the following simulations, firstly a magnetic structure needs to be created. This magnetic structure can then be examined by the desired simulated techniques. There are two main ways used here to produce these magnetic structures: analytically, or through micromagnetic simulations.

4.2.1 Analytical

If the analytical form of the magnetic structure to be simulated is known then a three-dimensional magnetisation array can be created with the corresponding magnetisation values. For example, as seen in Sec. 2.3, from symmetry the magnetisation of an isolated skyrmion can be written in Cartesian coordinates by parameterisation in cylindrical polar coordinates

$$\mathbf{M}(\mathbf{x}) = \sin \theta(\rho) \cos \Phi(\phi) \hat{x} + \sin \theta(\rho) \sin \Phi(\phi) \hat{y} + \cos \theta(\rho) \hat{z}, \quad (4.1)$$

where ρ and ϕ are respectively the radius and the polar angle in polar coordinates [37]. $\theta(\rho)$ and $\Phi(\phi)$ are functions that describe how the magnetisation varies as a function of ρ and ϕ respectively. One of the simplest solutions for $\Phi(\phi)$ can be represented in terms of the skyrmion number n and a phase γ

$$\Phi(\phi) = n\phi + \gamma. \quad (4.2)$$

Hence, for an isolated Bloch skyrmion with $n = 1$, $\gamma = \pi/2$, and a simple $\theta(\rho) = \pi \exp\{(-\rho/\rho_0)\}$ where $\rho_0 = 100$ nm the magnetisation structure is depicted in Fig. 4.1. Equation 4.2 enables simulations of other topological solutions such as, a Néel skyrmion which can be created by setting $n = 1$, $\gamma = 0$, an antiskyrmion with $n = -1$, $\gamma = 0$, and a biskyrmion with $n = 1$, $\gamma = 0$. Each of these are shown in Fig. 4.1.

This analytical solution assumes that there is no dependence of the magnet-

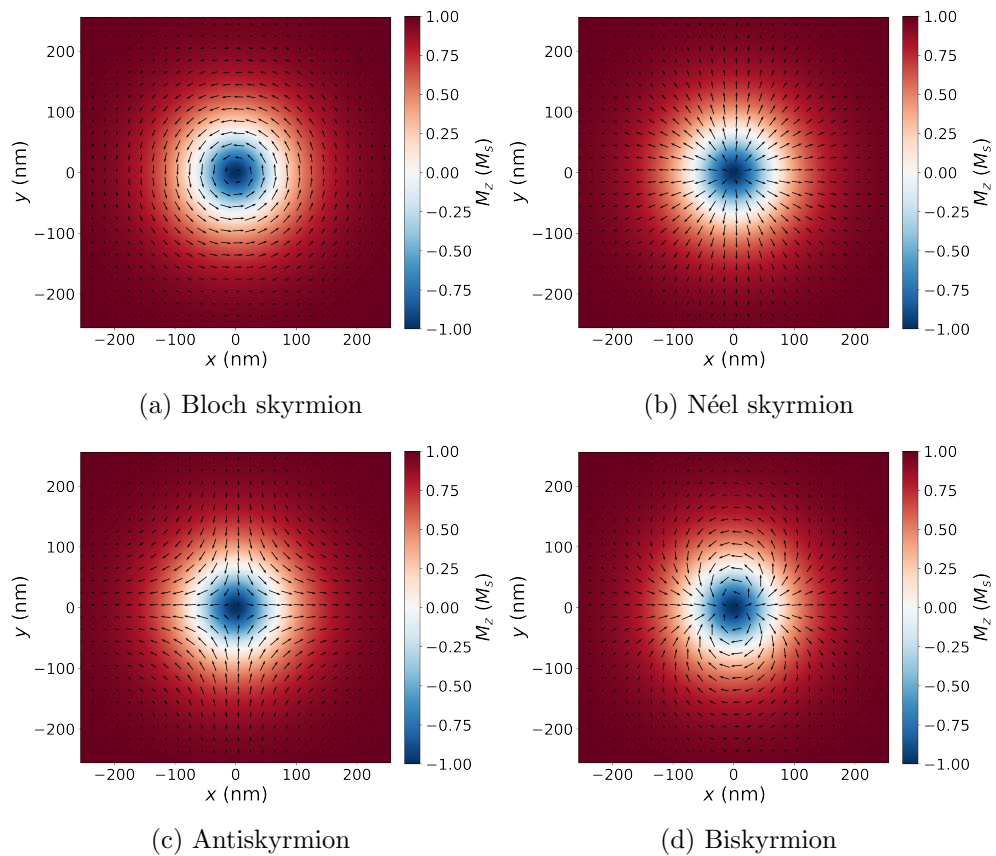


Figure 4.1: Analytical skyrmions with colour map showing M_z component of magnetisation and arrows depicting the in-plane magnetisation.

isation in the samples z direction due to the parameterisation in cylindrical polar coordinates. In fact, while a good first approximation this has been shown to be not entirely accurate as skyrmions and their magnetic structure can bend and twist breaking this symmetry [79, 80]. This means to more accurately describe skyrmions, software such as Ubermag [77] can be used to run micromagnetic simulations to produce a more realistic magnetic structure.

4.2.2 Ubermag

The micromagnetic simulation software Ubermag [77] is a prime example of a powerful software to generate three-dimensional magnetisation structures. Section 2.1.2 describes in detail how micromagnetics work, but in summary with just a few material parameters such as exchange, DMI, anisotropy, and saturation magnetisation, realistic magnetic structures can be created.

4.2.3 Rotations

The simulated magnetic structures mentioned so far have been created on Cartesian grids in the sample's reference frame. Experimental simulations are defined in the experimental reference frame so, unless the sample's axis are congruent with the experimental axis, rotations will be needed to be performed to move from the sample reference frame to the instrument reference frame. To make sure rotations do not place the sample being rotated outside of the viewing region, a buffer of zeros should be added surrounding the object. The rotations are given in terms of extrinsic rotations, as these are what are most commonly used with apparatus such as electron microscopes. The rotation matrix R of the magnetisation vector for rotations about the x , y , and z axis is given by

$$R_x = \begin{bmatrix} 1 & 0 & 0 \\ 0 & \cos(\theta_x) & \sin(\theta_x) \\ 0 & -\sin(\theta_x) & \cos(\theta_x) \end{bmatrix}, \quad (4.3)$$

$$R_y = \begin{bmatrix} \cos(\theta_y) & 0 & \sin(\theta_y) \\ 0 & 1 & 0 \\ -\sin(\theta_y) & 0 & \cos(\theta_y) \end{bmatrix}, \quad (4.4)$$

$$R_z = \begin{bmatrix} \cos(\theta_z) & -\sin(\theta_z) & 0 \\ \sin(\theta_z) & \cos(\theta_z) & 0 \\ 0 & 0 & 1 \end{bmatrix}, \quad (4.5)$$

where

$$R_{rot} = R_z \cdot R_y \cdot R_x. \quad (4.6)$$

This can be applied to the magnetisation vectors as $v_{rot} = R_{rot} \cdot v$. The positions of each of the vectors are rotated to are calculated using rotations of arrays.

Figure 4.2 shows a pre- and post- rotated magnetic structure of an anti-skyrmion in a $100 \times 100 \times 100$ nm box. Both the magnetisation vector and the box itself can be seen to have been rotated.

4.3 Lorentz Transmission Electron Microscopy

Lorentz Transmission Electron Microscopy (LTEM) is an increasingly popular method for investigating magnetic structures in thin lamellar of magnetic materials [14, 81, 82]. Details of this technique are given in Sec. 3.11.

4.3.1 Theory

The set up of a Transmission Electron Microscope is shown in Fig. 3.8 in Sec. 3.11. A parallel electron beam is incident on a thin lamellar of sample. Due to the charge of the electrons, they feel the Lorentz force as they travel through the electric and magnetic fields produced by the sample given by,

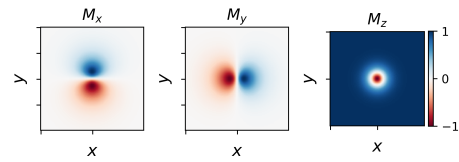
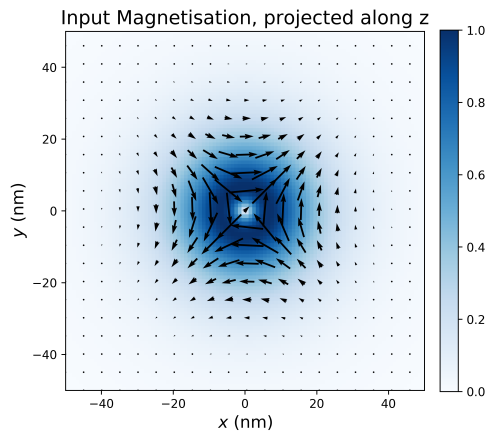
$$\mathbf{F} = -e(\mathbf{E} + \mathbf{v} \times \mathbf{B}), \quad (4.7)$$

where e is the charge on an electron, \mathbf{E} is the electric field, \mathbf{v} is the velocity of the electrons, and \mathbf{B} is the magnetic flux density. As this study is only interested in the contrast in images produced due to the magnetic textures in the sample, only the Lorentz force due the magnetic flux density will be examined,

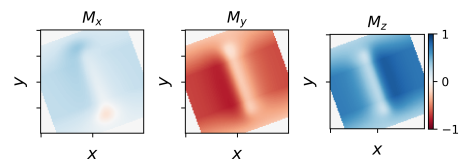
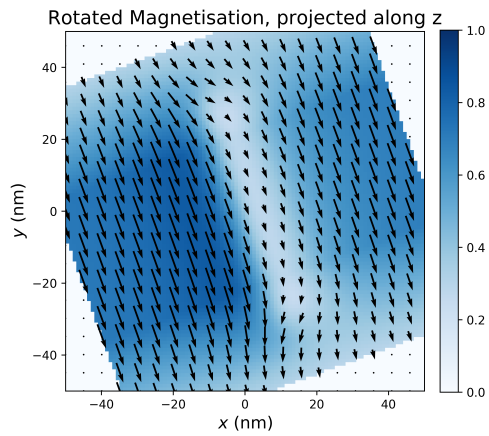
$$\mathbf{F}_B = -e\mathbf{v} \times \mathbf{B}. \quad (4.8)$$

It is worth noting that as the Lorentz force depends on $\mathbf{v} \times \mathbf{B}$ there is no force along direction of travel of the electron beam, hence Lorentz microscopy is only sensitive to the in-plane magnetic field i.e. the magnetic field perpendicular to the beam.

A commonly used example of the deflection of electrons in a TEM due to in-plane magnetic domains in a sample is shown in Fig. 4.3. It can be seen that the deflection of the electron beam by the magnetic domains in the sample causing a convergent and divergent sections of the beam. The electromagnetic projector lenses, situated below the sample, deflect the electrons to reconstruct the beam to hit viewing plane in the same state as it exited the sample plane. This means that when in-focus there is no magnetic contrast but if the viewing



(a) Initial magnetisation.



(b) Rotated by $\theta_x = 45$ and $\theta_z = 20$.

Figure 4.2: Initial and rotated magnetisation structure of an antiskyrmion in a $100 \times 100 \times 100$ nm box.

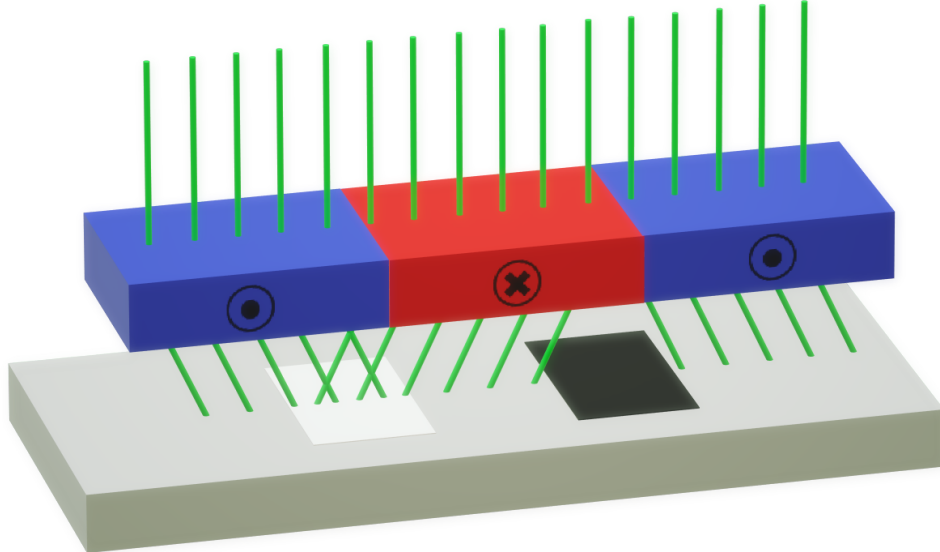


Figure 4.3: Diagram of an electron beam (green) travelling downwards through a magnetic sample with in-plane magnetic domains and creating bright and dark contrast on the image plane where the domain walls are situated.

plane is moved out-of-focus the the convergences and divergences of the electron beam manifesting as areas of high and low intensity.

Formalising this phenomena mathematically to create the experimental reference frame in a Cartesian coordinate system can be achieved by describing the electrons as a plane wave travelling along the optic axis which is defined to be in the z direction

$$\psi(\mathbf{x}) = A e^{i\alpha} = A(\mathbf{x}) e^{i[\phi(\mathbf{x}) + 2\pi k_z z]}, \quad (4.9)$$

with amplitude $A(\mathbf{x})$ and phase shift $\phi(\mathbf{x})$. The wavefunction located at the plane at the bottom of the sample can be defined as the sample exit wavefunction, which can be designated to occur at $z = 0$,

$$\psi_0(\mathbf{x}) \equiv \psi(x, y, z = 0). \quad (4.10)$$

Using the non-relativistic Schrödinger equation for electrons travelling through a magnetic field with relativistic corrections for wavelength and mass of the electron. The phase shift experienced by the electrons as they travel through

the sample due to the magnetic contribution is

$$\phi_m(x, y) = -\frac{2\pi e}{h} \int_{-\infty}^{\infty} A_z(x, y, z) dz, \quad (4.11)$$

where h is Planck's constant and \mathbf{A} is the magnetic vector potential, as defined in Ref. [83]. This integral corresponds to a projection of A_z along the z direction. Taking the Fourier transform of the magnetic phase shift and using the Fourier slice theorem leads to the relation

$$\tilde{\phi}_m(k_x, k_y) = -\frac{2\pi e}{h} \tilde{A}_z(k_x, k_y, 0). \quad (4.12)$$

To calculate the magnetic vector potential of the sample firstly the magnetic vector potential solution for a single classical dipole can be examined

$$\mathbf{A}(\mathbf{r}) = \frac{\mu_0}{4\pi} \left(\frac{\mathbf{m} \times \mathbf{r}}{|\mathbf{r}|^3} \right), \quad (4.13)$$

where \mathbf{r} is the vector from the centre of the dipole and μ_0 is the permeability of free space [83]. In the limit of continuous magnetisation the classical dipole expression can be extended to

$$\mathbf{A}(\mathbf{r}) = \frac{\mu_0}{4\pi} \int \mathbf{M}(\mathbf{R}) \times \left(\frac{\mathbf{r} - \mathbf{R}}{|\mathbf{r} - \mathbf{R}|^3} \right) d^3\mathbf{R}. \quad (4.14)$$

It is worth noting that this is related to Coulomb gauge. Examination of the structure of the equation reveals that this is a convolution between the magnetisation and the position, hence in Fourier space this convolution becomes a multiplication. The Fourier transform is the magnetic vector potential [84] can then be calculated to be

$$\tilde{\mathbf{A}}(\mathbf{k}) = -\frac{i\mu_0}{2\pi} \frac{\tilde{\mathbf{M}}(\mathbf{k}) \times \mathbf{k}}{k^2}. \quad (4.15)$$

As from Eqn. 4.12 only the z component of the \tilde{A}_z is required because of the cross-product in Eqn. 4.15 this will only depend on the in-plane components of $\tilde{\mathbf{M}}$ and \mathbf{k} , hence they can be denoted as $\tilde{\mathbf{M}}_{\perp}$ and \mathbf{k}_{\perp} . Recognising that in Eqn. 4.12 $k_z = 0$ therefore $\tilde{\mathbf{M}}(k_x, k_y, 0)$ which is equivalent to a integral over the z -direction i.e. the projection along the path of the electron beam

$$M_I(x, y) = \int_{-\infty}^{\infty} M(x, y, z) dz. \quad (4.16)$$

Rather than the integral, it is sometimes simplified in terms of a projected magnetisation $M_p(x, y)$ where

$$M_p(x, y)t = M_I(x, y) \quad (4.17)$$

and t is the thickness of the magnetic sample, considering in some cases the thickness can be spatially dependant. Equation 4.12 [84] can therefore be rewritten as

$$\tilde{\phi}_m(k_x, k_y) = \frac{ie\mu_0}{h} \frac{[\widetilde{\mathbf{M}}_I(k_x, k_y) \times \mathbf{k}_\perp]_z}{k_\perp^2}. \quad (4.18)$$

This expression gives a singularity when $k_\perp^2 = 0$ which cannot be handled computationally therefore a Tikhonov filter can be used to ensure the values remain finite [85]. The Tikhonov filter acts to change

$$\frac{1}{k^2} \xrightarrow{\text{Filter}} \frac{k^2}{(k^2 + k_c^2)^2} \quad (4.19)$$

where k_c is the radius of the filter. This radius should be kept small but non-zero to make sure to effect to the calculated phase is minimal.

$$\tilde{\phi}_m(k_x, k_y) = \frac{ie\mu_0 k_\perp^2}{h} \frac{[\widetilde{\mathbf{M}}_I(k_x, k_y) \times \mathbf{k}_\perp]_z}{(k_\perp^2 + k_c^2)^2}. \quad (4.20)$$

This phase shift can be used to create the sample exit wavefunction, as given in Eqn. 4.10. To propagate this wavefunction through space in an electron microscope the Contrast Transfer Function (CTF) can be used, which is defined in Fourier space as [86]

$$\tilde{T}(\mathbf{k}) = e^{-\gamma k^2}, \quad (4.21)$$

$$\gamma = -2i\pi\lambda\Delta f + \frac{1}{2}i\pi C_s \lambda^3 k^2. \quad (4.22)$$

γ is created out of two components, the first $2i\pi\lambda\Delta f$ depends of the relativistic wavelength of the electrons and the defocus Δf of the objective lens. This is equivalent to propagating the wavefunction through free-space by Δf . The second term $\frac{1}{2}i\pi C_s \lambda^3 k^2$ originates from the spherical aberration of the objective lens C_s . The CTF is then convolved with the sample exit wavefunction, defined in Eqn. 4.10, to give the wavefunction at specific defocus

$$\psi_{\Delta f} = \psi_0 * T, \quad (4.23)$$

$$\tilde{\psi}_{\Delta f} = \tilde{\psi}_0 \tilde{T}(\mathbf{k}), \quad (4.24)$$

$$\tilde{\psi}_{\Delta f} = \tilde{\psi}_0 e^{2i\pi k^2(-\frac{1}{2}\lambda\Delta f + \frac{1}{4}C_s \lambda^3 k^2)}. \quad (4.25)$$

The image at a specific defocus is then given by

$$I_{\Delta f} = |\psi_{\Delta f}|^2. \quad (4.26)$$

From the phase of the electrons determined other useful quantities can be

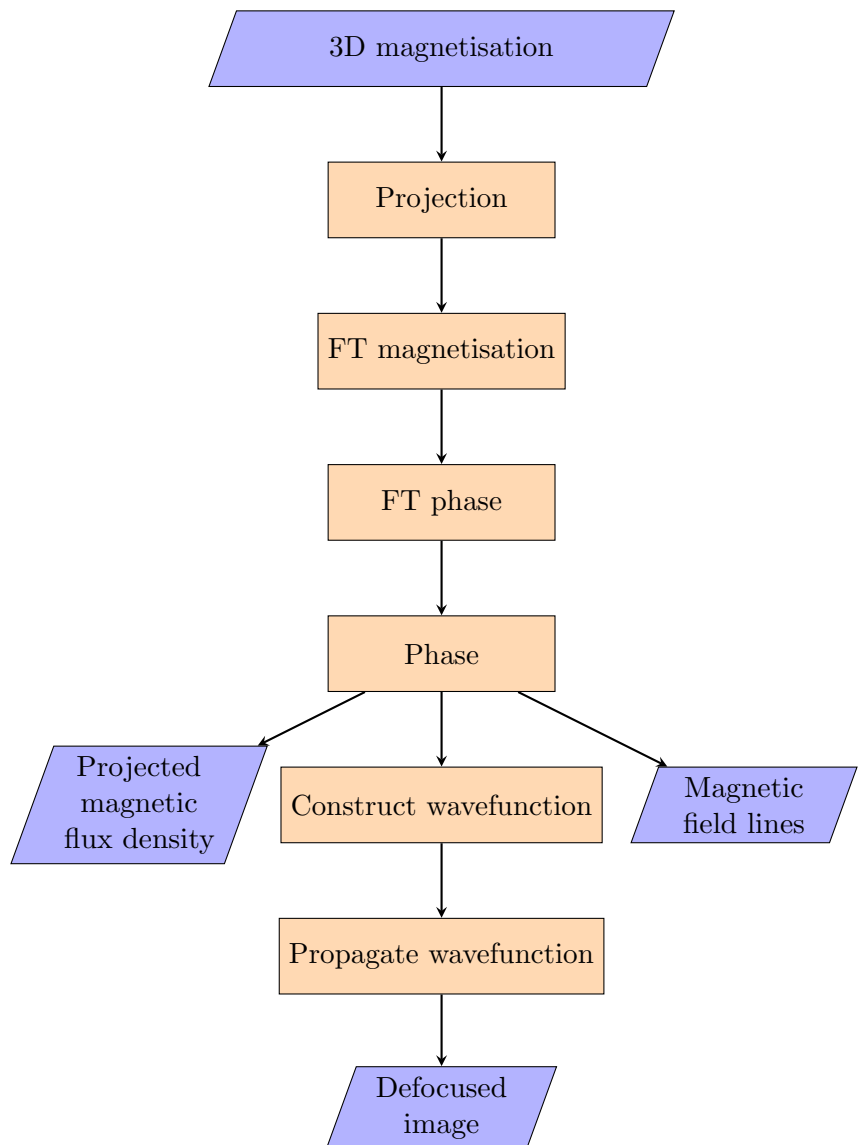


Figure 4.4: Flow chart of data analysis process from the input of a three-dimensional magnetisation to the outputs of projected magnetic flux density, magnetic field lines, and defocus imaging.

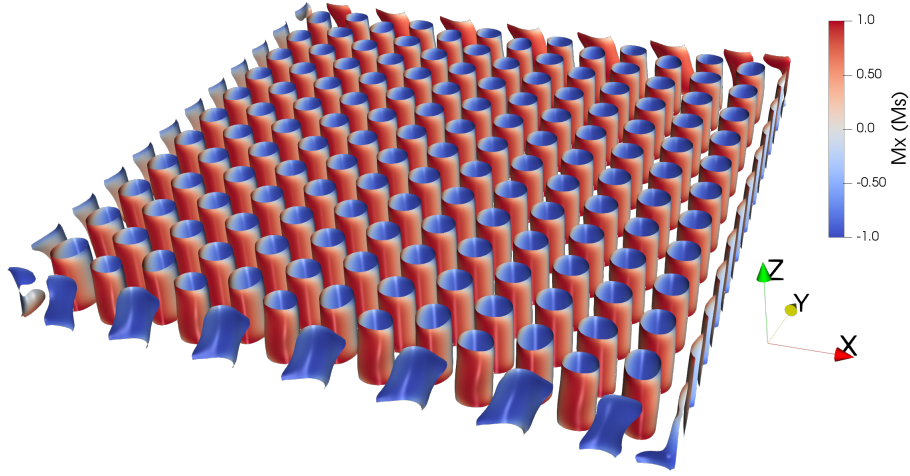


Figure 4.5: Micromagnetic simulation of a Bloch skyrmion lattice in a $1000 \times 1000 \times 100$ nm region with a resolution of 4 nm. The $M_z = 0$ contours are plotted as surfaces and with the M_x component of the magnetisation.

calculated such as the projected magnetic flux density \mathbf{B}_\perp . This can be used to compare against the results from electron holography, as it calculates the phase and hence \mathbf{B}_\perp is reconstructed. The \mathbf{B}_\perp can be calculated [84] from

$$\mathbf{B}_\perp = \frac{\Phi_0}{\pi t} \begin{pmatrix} -\partial/\partial y \\ \partial/\partial x \end{pmatrix} \phi_m, \quad (4.27)$$

which can be derived from relating the magnetic flux density to the phase via the magnetic vector potential. Field lines follow lines of constant magnetic flux density, hence taking the cosine of the phase highlights these contours. To change the density of the contours a phase amplification factor pa can be used to multiply the phase

$$\cos(pa\phi). \quad (4.28)$$

Using this theory for any given magnetisation structure a python programme has been written to calculate the expected image and phase from LTEM along with \mathbf{B}_\perp and the cosine of the phase

4.3.2 Implementation

This section will systematically walk through the Python implementation of the theory to produce LTEM simulations. Up to date versions of the code will be integrated with Ubermag [77]. Figure 4.4 depicts a flow chart of the

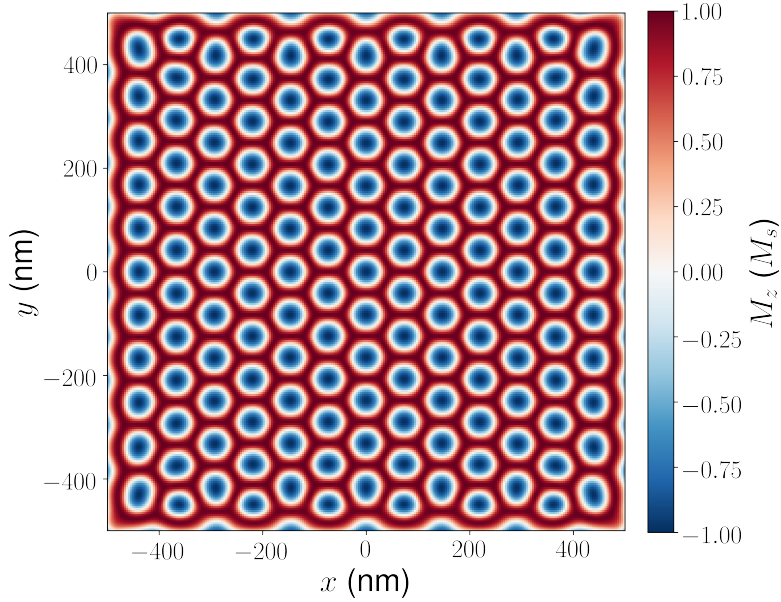


Figure 4.6: Projection along the z direction of the averaged M_z component of magnetisation.

processes enabling creation of the projected magnetic flux density, the field lines, and defocus images.

Figure 4.5 shows a three-dimensional magnetisation array created by micromagnetic simulations of a Bloch skyrmion lattice. These simulations were carried out on a $1000 \times 1000 \times 100$ nm region with a resolution of 4 nm. LTEM simulations will be performed with the beam aligned along the z direction, i.e. when the sample and experimental reference frames are the same.

Firstly, the magnetisation can be projected along the beam direction as only the plane perpendicular to the beam is needed, as shown in Eqn. 4.10. Figure 4.6 shows the z component of the projected magnetisation. The hexagonal lattice of skyrmions can be seen with the negative centre of the skyrmions in blue surrounded by a positive magnetisation state.

Taking the Fourier transform of M_x and M_y and using Eqn. 4.20 calculation of the Fourier transform of the phase as shown in Fig. 4.7. A hexagonal pattern can be seen indicating the hexagonal periodicity of the skyrmion lattice. The faint streaks in the square formation occur from the finite size and shape of the simulation box. Plotting the Tikhonov filter shows the size and shape of the filter, allowing a check that the filter is an appropriate size and not interfering with any features.

Taking the inverse Fourier transform of $\tilde{\phi}_m$ gives the phase shown in Fig. 4.8. This shows the phase shift of the electrons as they pass through the sample. A negative phase shift can be seen in the centre of the skyrmions and a positive phase shift the surrounding area.

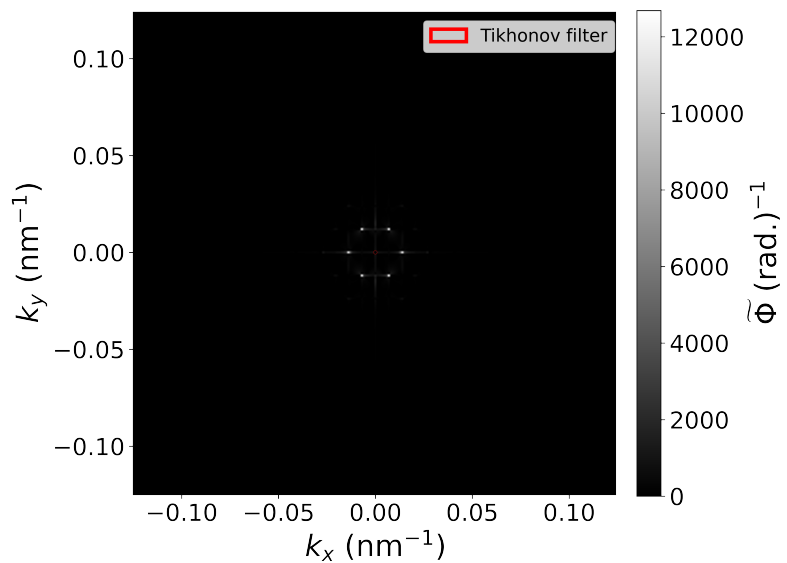


Figure 4.7: Fourier transform of the phase of the electrons. The small red circle in the centre shows the size of the Tikhonov filter.

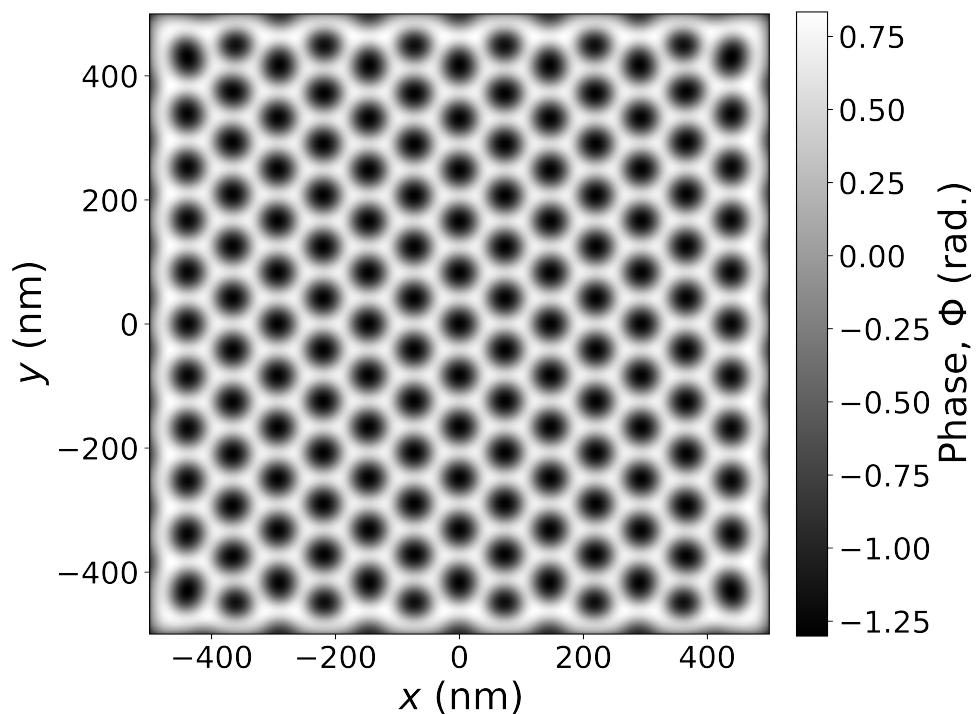


Figure 4.8: Phase of the electrons after travelling through the magnetic structure.

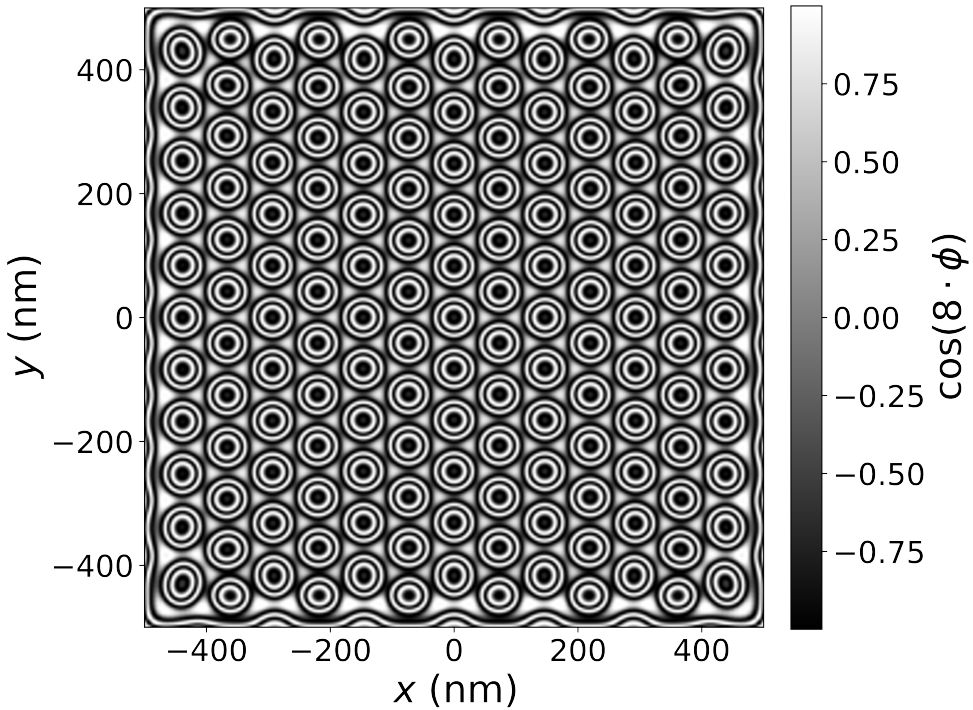


Figure 4.9: Cosine of the phase with a phase amplification factor of 8 i.e. $\cos(8\phi)$.

Once the phase of the electrons has been calculated the cosine of the phase give the contours of the magnetic field. If the phase is small it can be multiplied by a constant known as the phase amplification factor pa , Eqn. 4.28, which allows denser spacing of field lines. Figure 4.9 shows the cosine of the phase with $pa = 8$ highlighting the concentric field lines around the skyrmions.

From the phase the projected magnetic flux density can also be calculated via Eqn. 4.27 to get the in-plane components of \mathbf{B} . Figure 4.10 shows the projected magnetic flux density over only the centre 200×200 nm of the simulation for purposes of clarity. The colour denotes the in-plane direction of the as shown in the inset of the figure with black denoting the out-of-plane direction. Arrows are given to corroborate the direction of \mathbf{B}_\perp .

To create the defocused image the phase can be used to calculate the sample exit wavefunction ψ_0 using Eqn. 4.10 to give

$$\psi_0 = e^{i\phi_m}. \quad (4.29)$$

Fourier transforming the sample exit wavefunction and multiplying with the CTF with a beam voltage of 300 kV, spherical aberration coefficient C_s of 8000 mm, and a defocus of $\Delta f = -0.2$ mm leads to the image shown in Fig. 4.11.

Comparing the simulated defocused image in Fig. 4.11a to actual LTEM

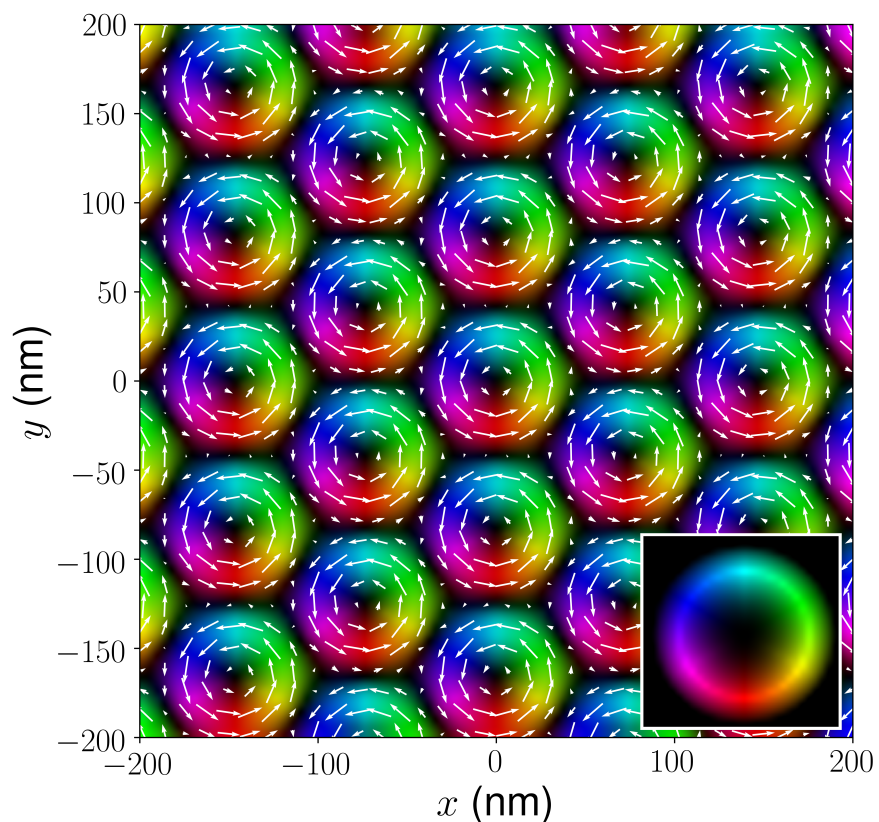
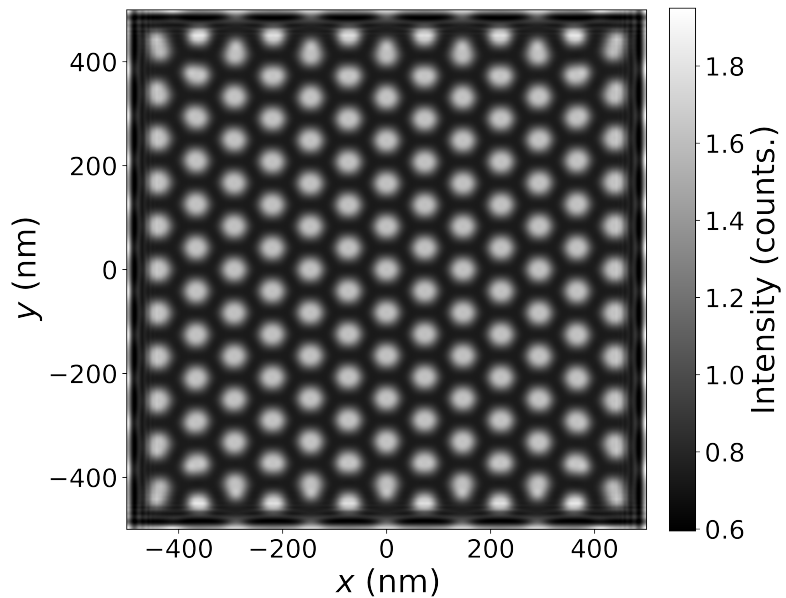
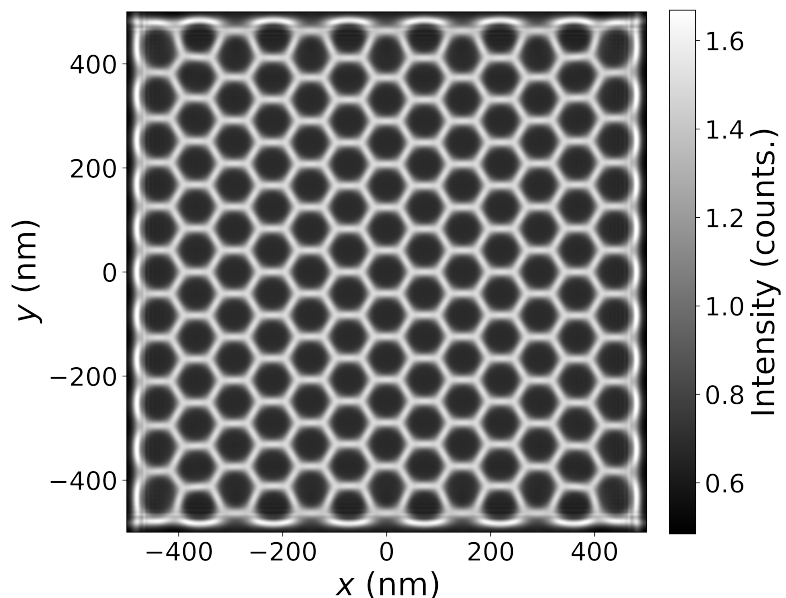


Figure 4.10: Projections of the magnetic flux density from the three-dimensional magnetic structure over a 200×200 nm area. The inset shows the colour wheel, where black represent out-of-plane magnetisation and the colour represents the direction of in-plane magnetisation.



(a) Defocus of $\Delta f = -0.2$ mm.



(b) Defocus of $\Delta f = +0.2$ mm.

Figure 4.11: Defocused image of three-dimensional magnetisation structure with a beam voltage of 300 kV and a spherical aberration coefficient C_s of 8000.

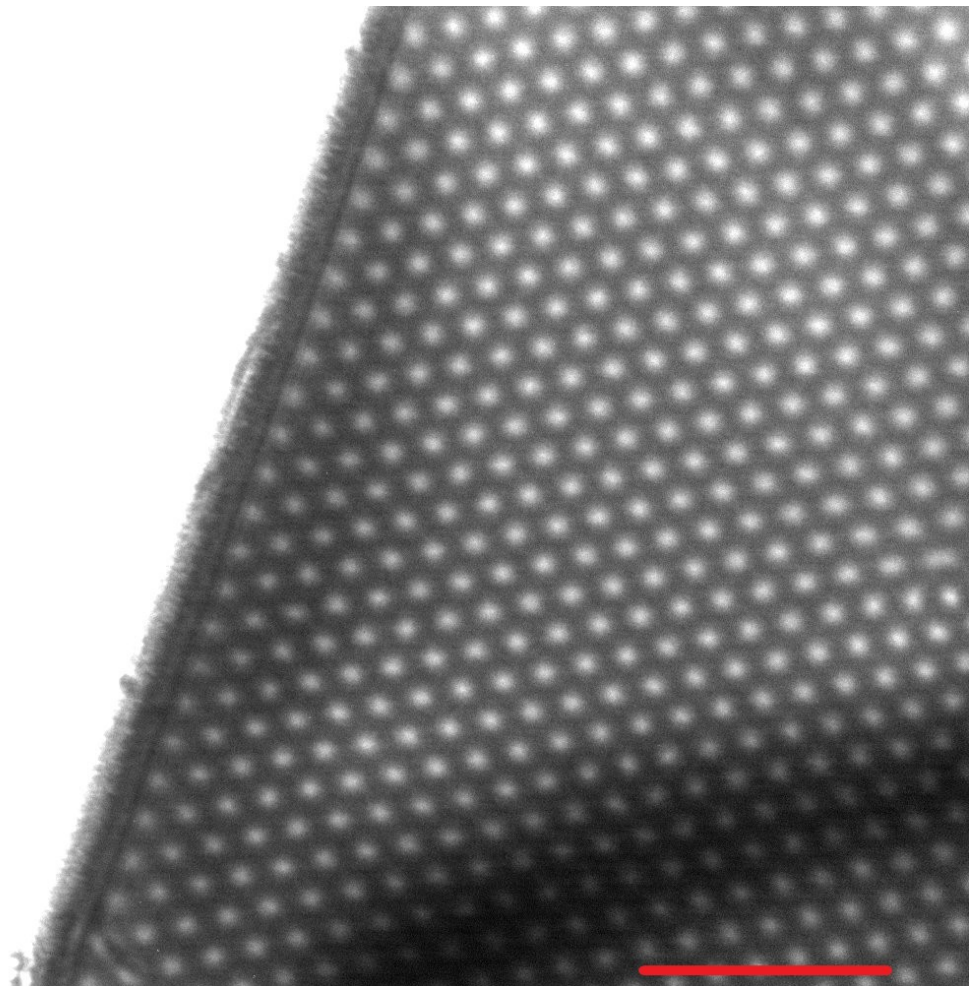


Figure 4.12: LTEM image of FeGe at 230 K in a vertical applied field of 115 mT with a 200 kV electron beam at a defocus of -0.294 mm. A red 500 nm bar is given for scale.

images taken on a lamella of FeGe in Fig. 4.12 shows excellent agreement with the theoretical predictions of a defocused image of skyrmion lattice. Both the simulated and actual image at negative defocus show the skyrmions as bright dots surrounded by a dark background with each spot representing a single Bloch skyrmion.

4.4 Magnetic Force Microscopy

Magnetic force microscopy (MFM) is a powerful technique for examining the magnetic field outside of a sample. The contrast in MFM images originates from the magnetic interaction between an oscillating cantilever and the samples magnetic field. It has a key role in the imaging of magnetism in thin films and samples with flat surfaces.

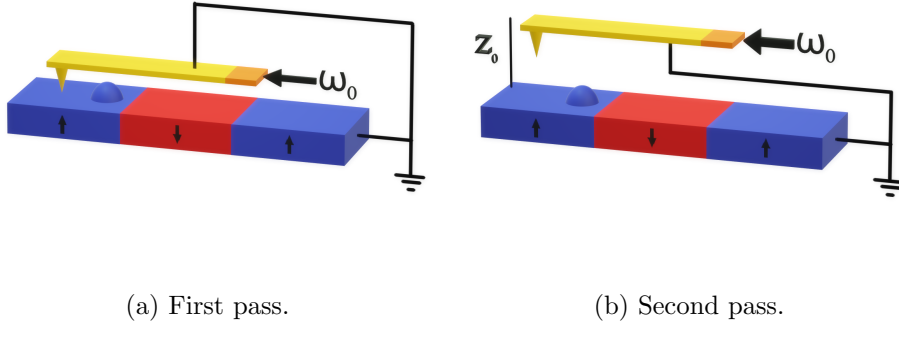


Figure 4.13: Schematics for an MFM in dual pass mode with resonant frequency ω_0 and lift off height for the second pass of z_0 .

4.4.1 Theory

Figure 4.13 shows the schematics for an MFM in dual pass mode. The cantilever in a dual pass MFM mode rasters across the same line scan twice, firstly mapping the topography by tapping along the surface at the resonant frequency ω_0 [87]. The second pass lifts the cantilever a set height from the sample surface, commonly referred to as h_l or z_0 , which is determined by the first pass and the phase shift $\Delta\phi$ of the resonance is then measured as the probe rasters across the sample. Here the experimental reference frame have been chosen to be in a Cartesian coordinate system with the z direction the axis along which the cantilever oscillates. From Newtons second law, the general damped harmonic oscillator equation in free space being driven by a time dependant force $F(t)$ can be written as

$$F(t) = m \frac{d^2\mathbf{x}(t)}{dt^2} + b \frac{d\mathbf{x}(t)}{dt} + k\mathbf{x}(t), \quad (4.30)$$

where m , k , and b are the mass, spring constant, and damping constant of the cantilever respectively. The spring constant is related to the resonant frequency by $k = m\omega_0^2$. Using the convention $b = m\omega_0/Q$ where Q is the quality factor of the cantilever and applying the experimental coordinate reference frame, Eqn. 4.30 can be rewritten as

$$F(t) = m \frac{d^2z(t)}{dt^2} + \frac{m\omega_0}{Q} \frac{dz(t)}{dt} + m\omega_0^2 z(t). \quad (4.31)$$

In the case where there is a sinusoidal driving force the the differential has general solution comprised of two parts

$$z(t) = z_t + z_{ss}, \quad (4.32)$$

where z_t is the transient part and z_{ss} is the steady state. Measurements taken using MFM are in the underdamped regime and measure using timescales longer than the relaxation time of system $Q/2\omega_0$ hence only the steady state solution will be examined. The sinusoidal driving force can be written in the form

$$F(t) = F_0 e^{i\omega t}, \quad (4.33)$$

where F_0 is a real number. Hence, if only take the real component is taken then it is $F_0 \cos(\omega t)$. The steady state solution of Eqn. 4.31 will also be of the form

$$z(t) = A e^{i(\omega t - \phi)}, \quad (4.34)$$

hence Eqn. 4.31 can be rewritten as

$$F_0 e^{i\omega t} = -m\omega^2 A e^{i(\omega t - \phi)} + i\omega \frac{m\omega_0}{Q} A e^{i(\omega t - \phi)} + m\omega_0^2 A e^{i(\omega t - \phi)}, \quad (4.35)$$

$$\frac{F_0}{Am} e^{i\phi} = \omega_0^2 - \omega^2 + i \frac{\omega\omega_0}{Q}. \quad (4.36)$$

Calculating the phase and amplitude of the complex right hand side of Eqn. 4.36 yields the amplitude and phase of the oscillation of the cantilever in free space,

$$A_f(\omega) = \frac{F_0}{m} \left[(\omega_0^2 - \omega^2)^2 + \left(\frac{\omega\omega_0}{Q} \right)^2 \right]^{-\frac{1}{2}}, \quad (4.37)$$

$$\phi_f(\omega) = \arctan \left(\frac{\omega\omega_0}{Q(\omega_0^2 - \omega^2)} \right). \quad (4.38)$$

Hence it can be seen, if the probe is driven at ω_0 then $\phi_f(\omega_0) = \pm\pi/2$.

Introducing an external force between the sample and the tip F_{ts} changes the tip response and introduces a phase shift between the new state and the state in free space. As the amplitude of the oscillations of the cantilever in the z direction are small compared to the equilibrium position of the cantilever z_0 , the tip sample force can be approximated with a Taylor expansion about z_0 ,

$$F_{ts} \approx \frac{dF_{ts}(z)}{dz} \Big|_{z=z_0} z(t). \quad (4.39)$$

Converting Eqn. 4.31 into the equation of motion of a damped harmonic oscillator while accounting for the tip sample force yields,

$$F(t) = m \frac{d^2 z(t)}{dt^2} + \frac{m\omega_0}{Q} \frac{dz(t)}{dt} + \left[m\omega_0^2 + \frac{dF_{ts}(z)}{dz} \Big|_{z=z_0} \right] z(t). \quad (4.40)$$

The solutions to this are also sinusoidal as given in Eqn. 4.34 but now with

$$A(\omega) = \frac{F_0}{m} \left[\left(\omega_0^2 - \omega^2 + m \frac{dF_{ts}(z)}{dz} \Big|_{z=z_0} \right)^2 + \left(\frac{\omega\omega_0}{Q} \right)^2 \right]^{-\frac{1}{2}}, \quad (4.41)$$

$$\phi(\omega) = \arctan \left(\frac{\omega\omega_0}{Q \left(\omega_0^2 - \omega^2 + m \frac{dF_{ts}(z)}{dz} \Big|_{z=z_0} \right)} \right). \quad (4.42)$$

If the probe is driven at it's resonant frequency Eqn. 4.42 can be written as

$$\phi(\omega_0) = \arctan \left(\frac{\omega_0^2}{Qm \frac{dF_{ts}(z)}{dz} \Big|_{z=z_0}} \right). \quad (4.43)$$

Hence by Taylor expanding the phase under the assumption that $m \frac{dF_{ts}(z)}{dz} \Big|_{z=z_0} \ll \omega_0^2$, the phase shift caused by F_{ts} is given by

$$\Delta\phi(\omega_0) = \phi_f(\omega_0) - \phi(\omega_0) \quad (4.44)$$

$$= \frac{\pi}{2} - \arctan \left(\frac{\omega_0^2}{Qm \frac{dF_{ts}(z)}{dz} \Big|_{z=z_0}} \right) \quad (4.45)$$

$$\approx \frac{Q}{k} \frac{dF_{ts}(z)}{dz} \Big|_{z=z_0} \quad (4.46)$$

The phase shift has the relation

$$\Delta\phi \propto \frac{dF_{ts}(z)}{dz}. \quad (4.47)$$

To calculate the force between the tip and the sample, the tip needs to be examined in greater detail.

The tip of an MFM is a complex magnetic object, which when placed in a magnetic field has a complex response. However, the force on a single magnetic moment by an external field is given by [88]

$$\mathbf{F} = (\mathbf{m} \cdot \nabla) \mathbf{B}. \quad (4.48)$$

The tip is made of many magnetic moments that interact with the stray field from the sample producing a force, isolating only the z component yields,

$$F_z = \mu_0 \frac{\partial}{\partial z} \iiint_{V_{\text{tip}}} \mathbf{M}_t(\mathbf{r}') \cdot \mathbf{H}_s(\mathbf{r} - \mathbf{r}') d\mathbf{r}'^3, \quad (4.49)$$

where this is an integral over the volume of the tip and $\mathbf{M}_t(\mathbf{r}')$ is the spatial

dependent magnetic moment of the tip. Most models assume a constant tip magnetisation $\mathbf{M}_t(\mathbf{r}') = \mathbf{M}_t$ leading to

$$F_z = \mu_0 \mathbf{M}_t \cdot \frac{\partial}{\partial z} \iiint_{V_{\text{tip}}} \mathbf{H}_s(\mathbf{r} - \mathbf{r}') d\mathbf{r}'^3. \quad (4.50)$$

With careful examination, the integral can be seen to take the form of a convolution leading to

$$F_z = \mu_0 \mathbf{M}_t \cdot \frac{\partial}{\partial z} (\mathbf{V}_f * \mathbf{H}_s(\mathbf{r})) \quad (4.51)$$

where \mathbf{V}_f is the volume function of the tip.

Putting this into the experimental coordinate system of the MFM leads to a phase shift of

$$\Delta\phi = \frac{Q\mu_0}{k} \mathbf{M}_t \cdot \left(\mathbf{V}_f * \frac{\partial^2 \mathbf{H}_s(\mathbf{r})}{\partial z^2} \right). \quad (4.52)$$

This is often given, under the assumption $\mathbf{M}_t = m_z$ acting at the central point of the tips magnetic volume hence \mathbf{V}_f can be described as a delta function positioned at central point of the tips magnetic volume

$$\Delta\phi = \frac{Q\mu_0 m_z}{k} \frac{\partial^2 \mathbf{H}_{sz}}{\partial z^2}. \quad (4.53)$$

Repeating this derivation, a more appropriate equation for the force on the MFM tip can be obtained by describing them using monopole and dipole interactions,

$$\mathbf{F} = (q + \mathbf{m} \cdot \nabla) \mathbf{B}, \quad (4.54)$$

where q is the effective magnetic monopole moment. Using this force in Eqn. 4.46 leads to the expression

$$\Delta\phi = \frac{Q\mu_0}{k} \left(q \frac{\partial \mathbf{H}_{sz}}{\partial z} + \mathbf{M}_t \cdot \frac{\partial^2 \mathbf{H}_s}{\partial z^2} \right). \quad (4.55)$$

It is worth noting this does not account for the finite shape and size of the tip but this can be rectified by convolving the phase with \mathbf{V}_f .

4.4.2 Fourier techniques

In a similar fashion to the calculations performed for LTEM the magnetic vector potential can be used

$$\mathbf{B} = \nabla \times \mathbf{A}, \quad (4.56)$$

where \mathbf{A} is given in Eqn. 4.14. As MFM can only perform outside the sample where $\mathbf{B} = \mu_0 \mathbf{H}$, hence

$$\mathbf{H} = \frac{1}{\mu_0} \nabla \times \mathbf{A}. \quad (4.57)$$

Taking the Fourier transform \mathbf{H} with $\tilde{\mathbf{A}}$ given in Eqn. 4.15,

$$\tilde{\mathbf{H}}(\mathbf{k}) = \frac{i}{\mu_0} \mathbf{k} \times \tilde{\mathbf{A}}(\mathbf{k}), \quad (4.58)$$

$$= \frac{1}{2\pi} \mathbf{k} \times \left[\frac{\tilde{\mathbf{M}}(\mathbf{k}) \times \mathbf{k}}{k^2} \right], \quad (4.59)$$

$$= \frac{1}{2\pi} \left[\tilde{\mathbf{M}}(\mathbf{k}) - \frac{(\tilde{\mathbf{M}}(\mathbf{k}) \cdot \mathbf{k}) \mathbf{k}}{k^2} \right]. \quad (4.60)$$

Using this to produce the differentials

$$\frac{\partial \mathbf{H}_s}{\partial z} \xrightarrow{FT} \frac{ik_z}{2\pi} \mathbf{k} \times \left[\frac{\tilde{\mathbf{M}}(\mathbf{k}) \times \mathbf{k}}{k^2} \right], \quad (4.61)$$

$$\frac{\partial^2 \mathbf{H}_s}{\partial z^2} \xrightarrow{FT} \frac{-k_z^2}{2\pi} \mathbf{k} \times \left[\frac{\tilde{\mathbf{M}}(\mathbf{k}) \times \mathbf{k}}{k^2} \right]. \quad (4.62)$$

Applying a Tikhonov filter, in a similar way as described as for LTEM Sec. 4.3, to ensure that the $k_\perp^2 = 0$ singularity is dealt with yields

$$\frac{\partial \mathbf{H}_s}{\partial z} \xrightarrow{FT} \frac{ik_z k^2}{2\pi} \mathbf{k} \times \left[\frac{\tilde{\mathbf{M}}(\mathbf{k}) \times \mathbf{k}}{(k_\perp^2 + k_c^2)^2} \right], \quad (4.63)$$

$$\frac{\partial^2 \mathbf{H}_s}{\partial z^2} \xrightarrow{FT} \frac{-k_z^2 k^2}{2\pi} \mathbf{k} \times \left[\frac{\tilde{\mathbf{M}}(\mathbf{k}) \times \mathbf{k}}{(k_\perp^2 + k_c^2)^2} \right]. \quad (4.64)$$

4.4.3 Implementation

The implementation of the MFM simulations is done in a very similar way to those of the LTEM simulations. In order to obtain an MFM image, the magnetisation have to be padded with layers of zero magnetisation vector above the sample by at least double the maximum scan height the MFM is wanted to be simulated. Here the magnetisation has been padded by 400 nm on in the z direction. Following this a three-dimensional Fourier transform of the magnetic structure is calculated and crossed with the \mathbf{k} vectors to obtain the Fourier transform of the magnetic field as given by Eqn. 4.60. The first and seconds order differentials with respect to H can be calculated using the k_z and performing an inverse Fourier transform as given by Eqn. 4.63 and 4.64. The phase shift experienced by the cantilever can be calculated using Eqn. 4.55. This gives the phase shift at every cell in the three-dimensional

simulation region.

For reasonable values of $Q = 650$ and $k = 4$ magnetic structure can be viewed under different conditions. Figure 4.14a shows the phase shift at a height of 40 nm above the surface with a tip magnetic moment of $M_z = 1 \times 10^{-13}$ emu. The magnetic skyrmions can clearly be seen as circular areas of higher phase shift. Figure 4.14b shows the phase shift at a height of 80 nm above the surface with a tip magnetic moment of $M_z = 1 \times 10^{-13}$ emu. Compared to Fig. 4.14a a clear difference can be seen in the magnitude of the phase shift but the features within the image remain the same. Figure 4.15 shows the phase shift at a height of 80 nm above the surface with a tip magnetic moment of $M_x = 1 \times 10^{-13}$ emu. In this configuration the tip magnetisation is only sensitive to the M_x for example, a domain wall rotating along one direction will appear opposite magnitude of phase shift compared to a domain wall rotating in the opposite direction. Figure 4.16 shows the phase shift at a height of 40 nm above the surface with a tip magnetic moment of $q = 1 \times 10^{-6}$ emu. The skyrmions have a similar shape but the contrast reduces.

4.5 Small Angle Neutron Scattering

Small Angle Neutron Scattering (SANS) is a reciprocal space technique allowing investigation into mesoscopic length scales, along with small angle x-ray scattering it is a key technique in many fields.

4.5.1 Theory

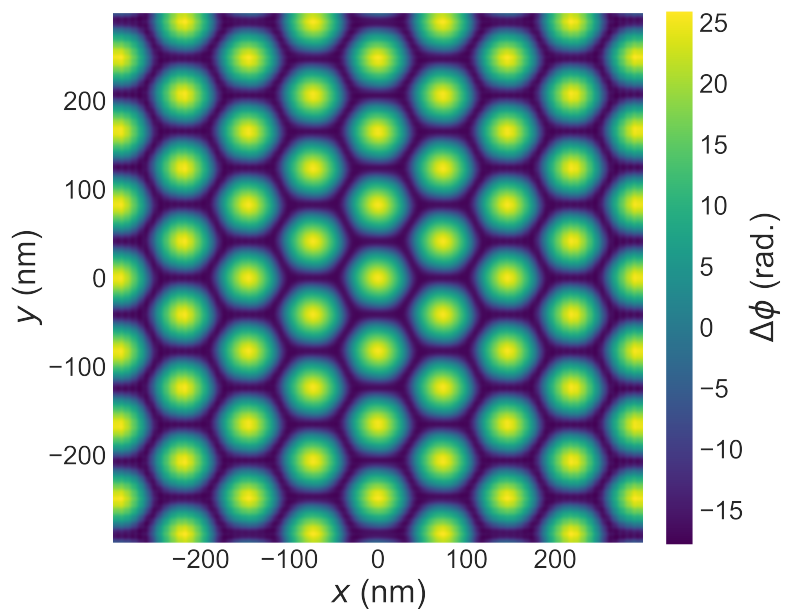
As a beam of neutrons travel through a material they interact with the nucleus of atoms and scatter. Due to the spin of the neutrons when they interact with a material they feel the presence of any magnetism. In SANS the atomic structure generally has a minimal impact hence the sample can be approximated by a continuous magnetisation vector field [89]. As diffraction is a reciprocal space technique, Fourier transforms can be used to predict the patterns obtained from different magnetic structures.

The differential scattering cross section $d\Sigma/d\Omega$ can be used as a function of the scattering vector \mathbf{q} to predict the pattern produced. To define this a Cartesian coordinates will be used with the beam direction along the z direction. The scattering can be calculated with the use of the magnetic interaction vector [89]

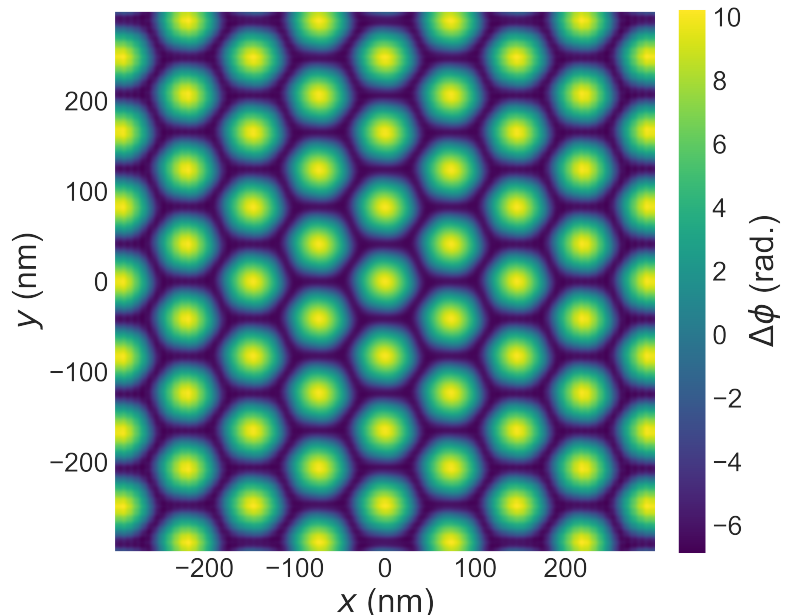
$$\mathbf{Q} = \hat{\mathbf{q}} \times [\hat{\mathbf{q}} \times \widetilde{\mathbf{M}}(\mathbf{q})], \quad (4.65)$$

$$= \hat{\mathbf{q}} [\hat{\mathbf{q}} \cdot \widetilde{\mathbf{M}}(\mathbf{q})] - \widetilde{\mathbf{M}}(\mathbf{q}), \quad (4.66)$$

$$= \widetilde{\mathbf{M}}_{\perp}(\mathbf{q}). \quad (4.67)$$



(a) 40 nm height.



(b) 80 nm height.

Figure 4.14: Phase shift of the cantilever at two different heights above the surface of the sample.

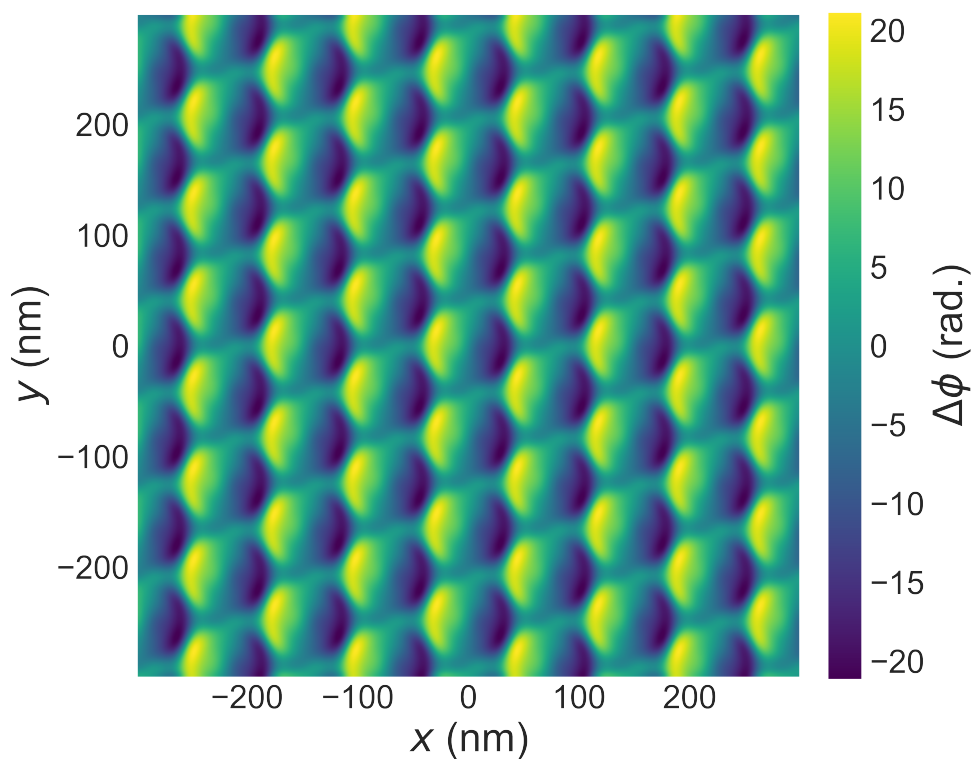


Figure 4.15: Phase shift of the cantilever when the tip is magnetised in the x direction.

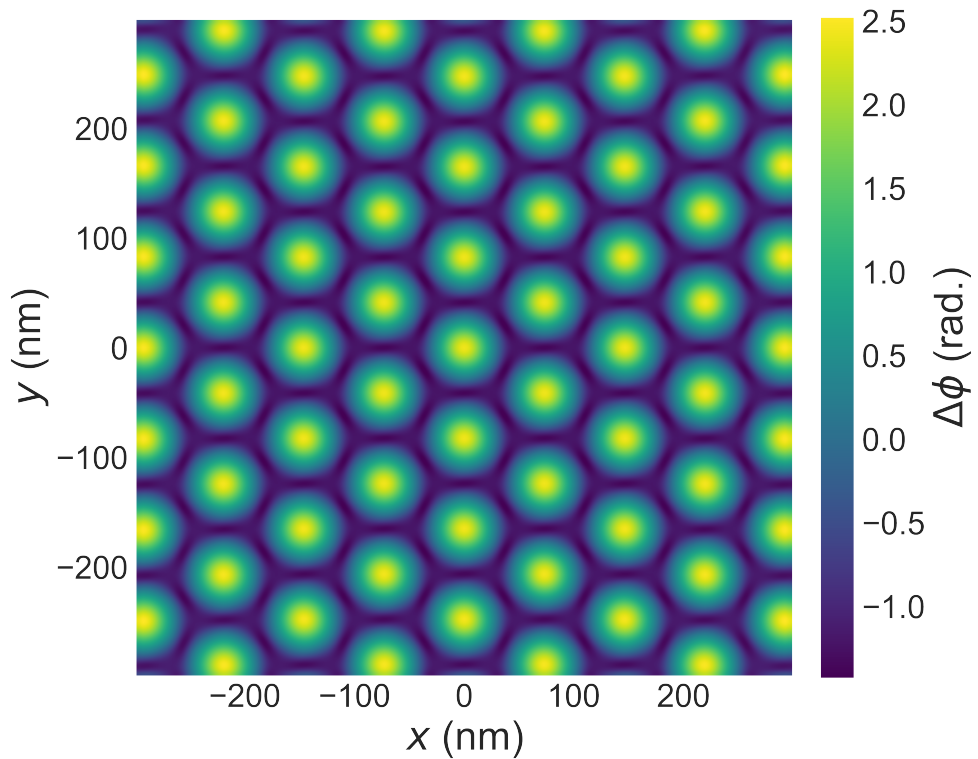


Figure 4.16: Phase shift of the cantilever due to a magnetic monopole moment.

Similarly to LTEM, the magnetisation can be projected along the beam direction to form a two-dimensional plane of magnetisation. There are 4 base scattering cross sections to be considered,

- $d\Sigma^{++}/d\Omega$ spin up non spin flip,
- $d\Sigma^{--}/d\Omega$ spin down non spin flip,
- $d\Sigma^{+-}/d\Omega$ spin up spin flip,
- $d\Sigma^{-+}/d\Omega$ spin down spin flip.

Uniaxial neutron-polarisation analysis (POLARIS), allows each of these cross sections to be identified individually. Half-polarised cross sections can be used to explain experiments with a polarised incident beam and no detection polarisation detection of the (SANSPOL)

$$\frac{d\Sigma^+}{d\Omega} = \frac{d\Sigma^{++}}{d\Omega} + \frac{d\Sigma^{+-}}{d\Omega}, \quad (4.68)$$

$$\frac{d\Sigma^-}{d\Omega} = \frac{d\Sigma^{--}}{d\Omega} + \frac{d\Sigma^{-+}}{d\Omega}. \quad (4.69)$$

For non-polarised SANS

$$\frac{d\Sigma}{d\Omega} = \frac{1}{2} \left(\frac{d\Sigma^+}{d\Omega} + \frac{d\Sigma^-}{d\Omega} \right), \quad (4.70)$$

$$= \frac{1}{2} \left(\frac{d\Sigma^{++}}{d\Omega} + \frac{d\Sigma^{--}}{d\Omega} + \frac{d\Sigma^{+-}}{d\Omega} + \frac{d\Sigma^{-+}}{d\Omega} \right). \quad (4.71)$$

Choosing an experimental reference frame with the beam incoming aligned and polarised along the z direction, the non-polarised SANS cross section is

$$\frac{d\Sigma}{d\Omega} \propto \|\widetilde{M}_x\| + \|\widetilde{M}_y\|. \quad (4.72)$$

4.5.2 Implementation

Using the magnetisation structure of a skyrmion lattice, as seen in Fig. 4.5 the unpolarised SANS pattern with a beam direction along the z direction in the sample reference frame can be simulated. Firstly, the magnetisation has to be projected along the beam direction to obtain a two-dimensional plane. The M_x and M_y components can then be Fourier transformed and the cross section calculated via Eqn. 4.72. Figure 4.17 shows the simulated SANS pattern. An obvious hexagonal pattern can be seen, showing underlying the periodicity of the hexagonal skyrmion lattice.

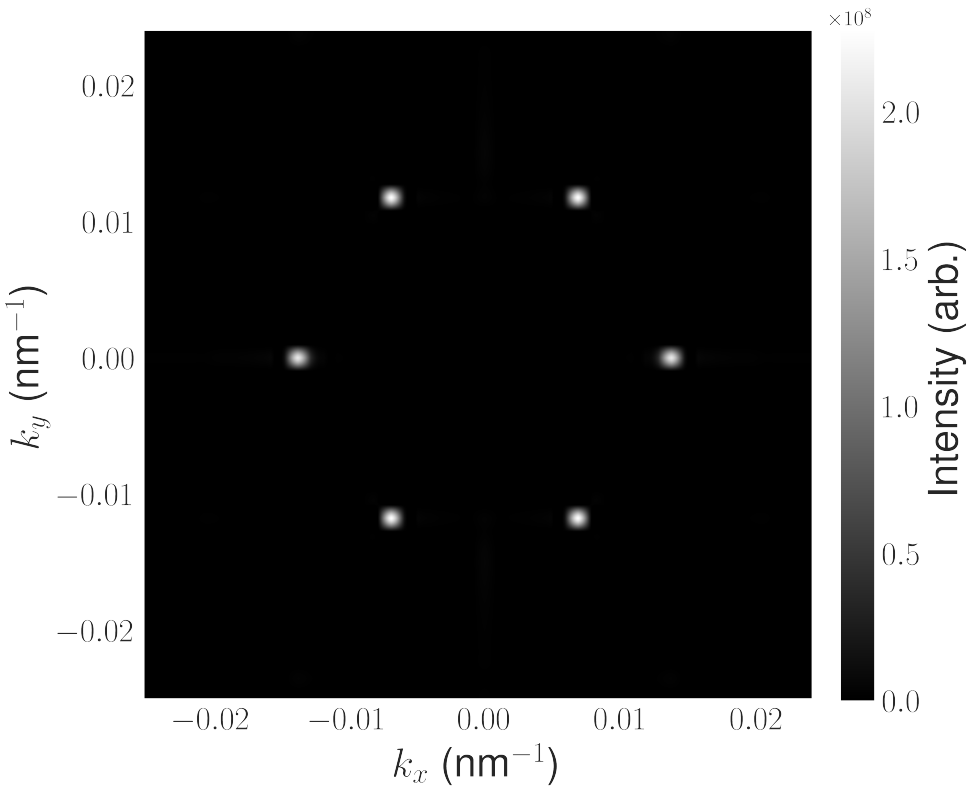


Figure 4.17: Simulated SANS pattern of a hexagonal skyrmion lattice.

4.6 X-ray Holography

X-ray holography uses circularly polarised x-rays tuned to the resonances of the magnetic atoms. These x-rays are directed through a slit with known diffraction pattern and a small aperture with a thin lamella of sample behind it. Deconvolution of the diffraction patterns of the slit and sample allows an image of the components of magnetisation perpendicular to the beam direction to be created. The magnetisation can be projected along the x-ray beam direction, which will be taken as the z direction in the sample reference frame. The z component of the projected magnetisation simply recreate the image from x-ray holography. For the hexagonal skyrmion lattice shown in Fig. 4.5 the holography image is shown in Fig. 4.6.

4.7 Limitations

As with most techniques, there are some limitations that should be considered prior using them. Most of the approaches outlined in this chapter use Fourier transforms as part of the method to calculate the image produced by the experimental technique. Due to the reciprocal relationship between real space and Fourier space; when simulating reciprocal space techniques, such as SANS,

the extent of the input magnetisation has to be considered as this will relate to the resolution in reciprocal space. This is as the larger the real space magnetisation, the better the resolution in reciprocal space. Likewise, the resolution of the magnetisation in real space will dictate the size of the reciprocal space examined.

When simulating real space techniques such as LTEM and MFM, parts of the calculation are performed in Fourier space. This causes a unique issue due to the periodic nature of Fourier transforms. This periodicity means that small artefacts can be created near the edges of the simulation window, however this can often be mitigated by using a buffer around the magnetisation. A clear example of this can be seen in simulations for MFM where when using a buffer above the sample to calculate the phase shift of the cantilever. This buffer has to be at minimum twice the lift of height that is desired to be simulated because, due to the periodicity of the Fourier technique, there will be a phase shift near the top edge of the simulation window which is effectively caused by the magnetisation at the bottom of the sample. Due to this, artefacts can be created if measuring too high without a reasonable buffer size.

4.8 Summary and Conclusions

In this chapter, the workings of a Python code to simulate a variety of experimental techniques have been detailed. Using a three-dimensional magnetic structure, the results of techniques such as Lorentz transmission electron microscopy, x-ray holography, magnetic force microscopy, and small angle neutron scattering have been able to be simulated. Even though there are some limitations that arise from the calculation methods used, these can often be mitigated against enabling the simulations to closely match the results of real world experiments. In the future, there is the possibility to add to the range of techniques that can be simulated along with directly integrating this code into micromagnetic software such as Ubermag. This will further bridge the gap between computational micromagnetic simulations and experiments, and can be used to inform real world experiments.